

Article

CuO/ZnO/CQDs@PAN Nanocomposites with Ternary Heterostructures for Enhancing Photocatalytic Performance

Huanhuan Xu [†], Peizhi Fan [†] and Lan Xu ^{*†} 

National Engineering Laboratory for Modern Silk, College of Textile and Engineering, Soochow University, Suzhou 215123, China

* Correspondence: lanxu@suda.edu.cn

† These authors contributed equally to the work.

Abstract: Photocatalysis is a green technology. In this paper, CuO/ZnO/carbon quantum dots (CQDs)@PAN nanocomposites with ternary heterostructures (CZC@PAN)—as high-performance environmentally friendly nanophotocatalysts—were prepared by electrospinning, heat treatment, and hydrothermal synthesis in sequence, and their practical applications were investigated by degrading methylene blue (MB). The synergistic effects of components in ternary heterostructures on the morphology, structure, and photocatalytic performance of CZC@PAN were analyzed, and their photocatalytic mechanism was further discussed. The results showed that due to the formation of p-n heterojunctions and the loading of CQDs and CZC@PAN had excellent photocatalytic degradation performance, and its photocatalytic degradation rate for MB reached 99.56% under natural sunlight for 4 h.

Keywords: nanofiber membrane; photocatalysis; heterostructure; degradation; carbon quantum dots



Citation: Xu, H.; Fan, P.; Xu, L. CuO/ZnO/CQDs@PAN Nanocomposites with Ternary Heterostructures for Enhancing Photocatalytic Performance. *Catalysts* **2023**, *13*, 110. <https://doi.org/10.3390/catal13010110>

Academic Editor: Sergey Nikitenko

Received: 25 November 2022

Revised: 30 December 2022

Accepted: 1 January 2023

Published: 4 January 2023



Copyright: © 2023 by the authors. Licensee MDPI, Basel, Switzerland. This article is an open access article distributed under the terms and conditions of the Creative Commons Attribution (CC BY) license (<https://creativecommons.org/licenses/by/4.0/>).

1. Introduction

Photocatalytic degradation technology can effectively eliminate organic pollutants in wastewater [1], and its core is photocatalysis [2]. Nano semiconductor photocatalysts—such as TiO₂, ZnO, Fe₂O₃ and ZnS [3–6]—have been widely regarded and studied due to their high efficiency, low energy consumption, non-toxicity, and harmlessness in wastewater treatment. ZnO is an n-type semiconductor, which has become a highly active photocatalyst due to its unique physicochemical properties [7–10]. However, ZnO with a wide bandgap can only absorb ultraviolet (UV) light, resulting in its low utilization of sunlight. Simultaneously, it has poor photocatalytic quantum efficiency due to the rapid recombination of photogenerated electrons and holes [11]. CuO is a p-type semiconductor with a narrow bandgap, which has a wide range of light absorption [12]. The combination of CuO and ZnO can form p-n heterojunctions, which can effectively separate the photogenerated electron–hole pairs to accelerate the photocatalytic reaction, and also extend the light response range of ZnO from the UV region to the visible light region [13].

Carbon quantum dots (CQDs), as a new type of fluorescent carbon nanomaterial, can be very useful components in the design of composite photocatalysts due to their unique optical properties [14–16]. Especially, their up-converted photoluminescence (PL) behavior can further extend the light utilization range of semiconductors, excite semiconductors to form more photogenerated electron–hole pairs, and enhance photoinduced electron transfer, thereby improving their photocatalytic degradation efficiency [17]. For example, the combination of CQDs with ZnO can convert the absorbed long-wavelength light into short-wavelength light, and excite ZnO to form more photogenerated electron–hole pairs, thus enhancing the photocatalytic activity of ZnO [18,19]. Similarly, the composites of CuO and CQDs can also enhance the photocatalytic degradation of dyes and organic pollutants under visible light [20]. In addition, due to the corrosion resistance of CQDs, the recycling rate of composite photocatalysts can be greatly improved. However, these composite

photocatalysts compounded with CQDs are mostly nanoparticles that are difficult to recycle and reuse [21–24].

Nanofiber membranes (NFMs) prepared by electrospinning technology have the advantages of large specific surface area, no secondary pollution, and being easy to recycle [25–28]. Therefore, in this paper, CuO/ZnO/CQDs@PAN nanophotocatalysts with ternary heterostructures (CZC@PAN) were prepared, characterized, and applied in the photocatalytic degradation of methylene blue (MB). Moreover, the effects of the addition of CQDs and the synergistic effects of components in ternary heterostructures on the photocatalytic degradation performance of photocatalysts were investigated. Meanwhile, the photocatalytic mechanism of CZC@PAN was further discussed and verified. As shown in Table 1, CZC@PAN has excellent photocatalytic degradation performance compared with other ZnO-based nanophotocatalysts. In addition, it was found that the nanoparticle-like photocatalysts had better degradation effects [29,30], but they are not easy to recover and reuse.

Table 1. Photocatalytic degradation activity of ZnO-based nanophotocatalysts.

Photocatalyst	Pollutants	Photocatalytic Degradation	Reference
NFMs loaded with CuO/ZnO	MB:10 mg/L	UV light: 60% for 3 h, 94.2% for 7 h	[5]
PAN/Ag/ZnO microporous membranes	Rhodamine B (RhB):10 mg/L	Visible light: 72% for 3 h	[8]
ZnO@CuO nanoparticles	methyl orange (MO)	UV light: 93.3% (MO) and	[29]
	MB	94.4% (MB) for 100 min	
CuO/ZnO nanoparticles	MB: 10 mg/L	Sunlight: 98% for 2 h	[30]
ZnO nanoparticles encapsulated NFMs	MO: 20 mg/L	UV light: 95% for 9 h	[31]
PAN-ZnO/Ag NFMs	MB: 5 mg/L	UV light: 85% for 2 h	[32]
Porous TiO ₂ /ZnO NFMs	MB: 12.8 mg/L	Xenon-lamp: 30% for 1 h	[33]
NFMs loaded with CuO/ZnO	MO:10 mg/L	UV light: 92.2% for 5 h	[34]
ZnO/CQDs nanoparticles	Benzene: 15.6 ppm	Visible light: 86% for 24 h	[35]
ZnO/CQDs nanoparticles	RhB	Visible light: 80% for 2 h	[36]
CZC@PAN NFMs	MB:10 mg/L	UV light: 92.38% for 1.5 h, Sunlight: 99.56% for 4 h	This work

2. Results and Discussion

2.1. Morphology and Structure Analysis

Cu(Ac)₂/Zn(Ac)₂/PAN-CNFMs had a smooth fiber surface (Figure 1a), while CZ-NPs-CNFMs had a considerable number of particles on the fiber surface (Figure 1b), which were probably CuO and ZnO nanoparticles generated by thermal decomposition of Cu(Ac)₂ and Zn(Ac)₂, respectively. Many lamellar crystals were grown on the fiber surface of CZ@PAN (Figure 1c) and CZC@PAN (Figure 1d) due to the formation of heterostructures during hydrothermal growth. However, the lamellar crystals on the fiber surface of CZC@PAN were smaller and denser due to the influence of CQDs on their growth. TEM image (Figure 1e) indicated that the nanosheets were formed on the fiber, and nearly spherical CQD nanoparticles were uniformly distributed on the nanosheets. HRTEM image (Figure 1f) showed that the lattice spacing of CuO, ZnO, and CQDs was 0.23 nm, 0.26 nm and 0.21 nm, respectively, corresponding to the (111) crystal plane of CuO, the (002) crystal plane of ZnO, and the (100) crystal plane of graphite phase. This showed that CQDs were successfully loaded on the CuO/ZnO heterostructure, generating a ternary CuO/ZnO/CQDs heterostructure. EDS results (Figure 1g) indicated that CZC@PAN mainly included C, O, Cu, and Zn, and all elements were uniformly distributed, confirming the existence and loading of CQDs on the surface of ZnO and CuO crystals, which was consistent with the TEM image analysis results. In addition, the element mapping still showed that the content of C element was lower than that of O, Cu, and Zn elements, which was due to the lower content of CQDs on the sample surface.

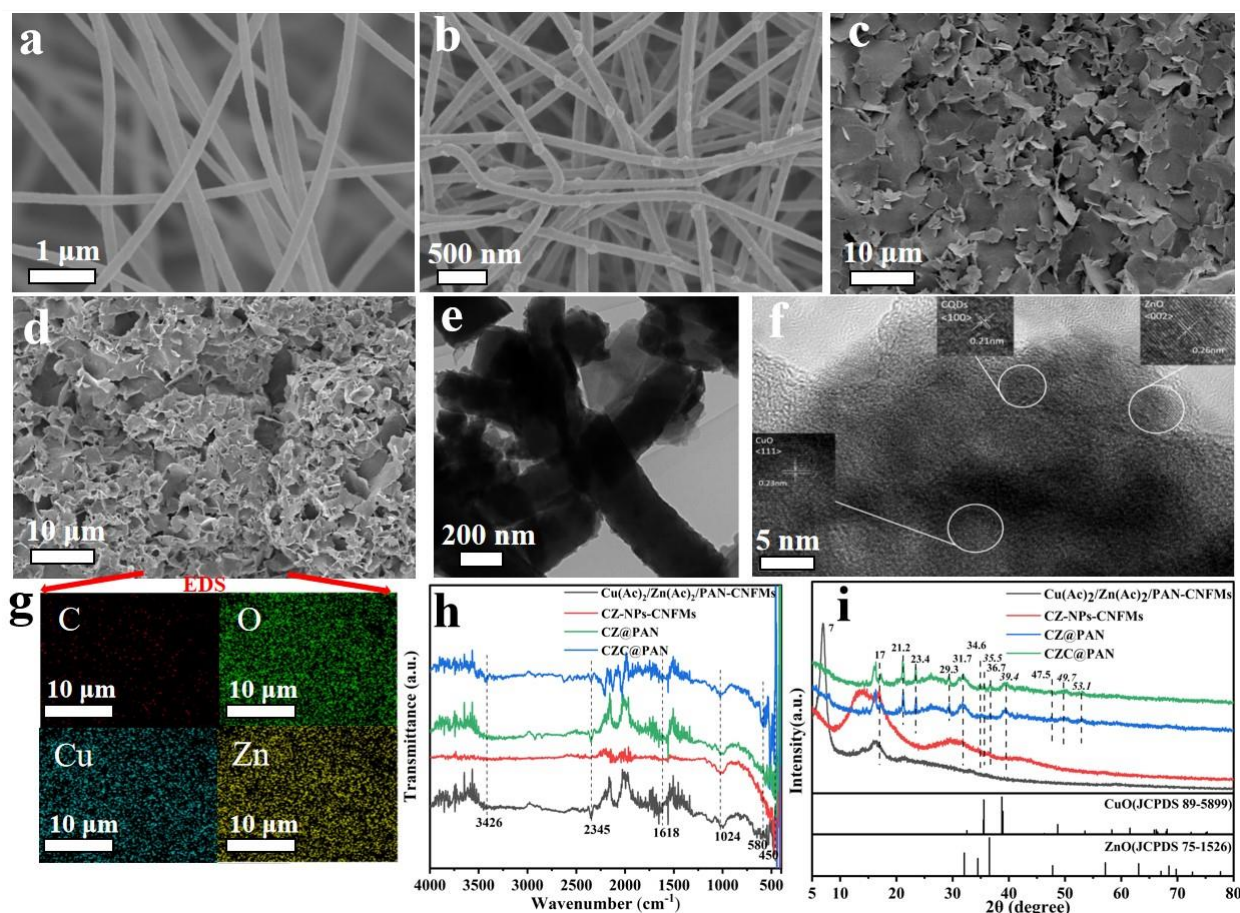


Figure 1. SEM image of $\text{Cu}(\text{Ac})_2/\text{Zn}(\text{Ac})_2/\text{PAN-CNFM}$ (a); SEM image of CZ-NPs-CNFMs (b); SEM image of CZ@PAN (c); SEM image (d), HRTEM image (e), TEM image (f), and EDS results (g) of CZC@PAN; FTIR patterns (h) and XRD spectra (i) of samples.

2.2. FTIR and XRD Analysis

In FTIR patterns (Figure 1h), all samples showed the absorption peaks at 2345 cm^{-1} , 1618 cm^{-1} , and 1024 cm^{-1} , separately assigning to the stretching vibration of nitrile group $\text{C}\equiv\text{N}$ in PAN, the vibrations of oxygen-containing groups $\text{C}=\text{O}$ and $\text{C}-\text{O}$. CZ-NPs-CNFMs, CZ@PAN and CZC@PAN all exhibited the absorption peaks at 450 cm^{-1} and 580 cm^{-1} , corresponding to the stretching vibrations of $\text{Zn}-\text{O}$ and $\text{Cu}-\text{O}$ bonds, respectively, due to the generation of ZnO and CuO [37–39]. The stretching vibration of $-\text{OH}$ was attributed to the broad absorption peak near 3426 cm^{-1} , which was more visible after loading CQDs. In XRD spectra (Figure 1i), $2\theta = 17^\circ$ related to the diffraction peaks of PAN, while $2\theta = 7^\circ$, 23.4° , 21.2° , and 29.3° corresponded to the diffraction peaks of $\text{Cu}(\text{Ac})_2$ and $\text{Zn}(\text{Ac})_2$ [40,41], which was caused by the incomplete decomposition of $\text{Cu}(\text{Ac})_2$ and $\text{Zn}(\text{Ac})_2$ due to the low heat treatment temperature. The diffraction peaks at 35.5° , 39.4° , 49.7° , and 53.1° corresponded to the (-111) , (111) , (-202) , and (020) crystal planes of CuO (JCPDS 89-5899), while the diffraction peaks at 31.7° , 34.6° , 36.7° , and 47.5° was the (100) , (002) , (101) , and (102) crystal planes of ZnO (JCPDS 75-1526). There were no apparent diffraction peaks of CQDs in the XRD spectrum of CZC@PAN due to the low amount of CQDs.

2.3. XPS Analysis and Mott–Schottky Test

In XPS survey spectra (Figure 2a), the surface components of samples were O, C, Cu, and Zn. The peaks at 284.8 eV, 286.2 eV, and 288.4 eV in the XPS spectra of C 1s (Figure 2b) corresponded to sp^2 ($\text{C}=\text{C}/\text{C}-\text{C}$), $\text{C}-\text{O}$, and carboxy COOR , respectively [20]. Comparing the two samples showed that the addition of CQDs had an impact on these peaks. The peaks near 530 and 532 eV in the XPS spectra of O 1s (Figure 2c) were assigned to O

in metal oxides and oxygen-containing functional groups, respectively. Compared with CZ@PAN, the oxygen-containing functional group peak of CZC@PAN shifted to 532.5 eV, showing that some Zn–O bonds in the sample had been converted to Zn–COO bonds, also confirming the presence of interaction between CuO/ZnO heterostructure and CQDs. XPS spectra of Cu 2p (Figure 2d) indicated that the energy level peaks of Cu 2p_{3/2} and Cu 2p_{1/2} for CZ@PAN were located at 933.5 eV and 953.5 eV, respectively. However, for CZC@PAN, the two peaks were separately located at 933.8 eV and 953.8 eV, showing a slight positive shift of 0.3 eV. In addition, both samples had two satellite peaks around 942 eV and 960 eV, illustrating that elemental Cu was in a divalent oxidation state [29]. XPS spectra of Zn 2p (Figure 2e) displayed double peaks at 1022 eV and 1045 eV, which belonged to Zn 2p_{3/2} and Zn 2p_{1/2}, respectively, indicating that the oxidation state of Zn on the surface of samples was +2 valence. In conclusion, the XPS analysis results exhibited the formation of CuO/ZnO/CQDs heterostructures, which were consistent with the XRD analysis results.

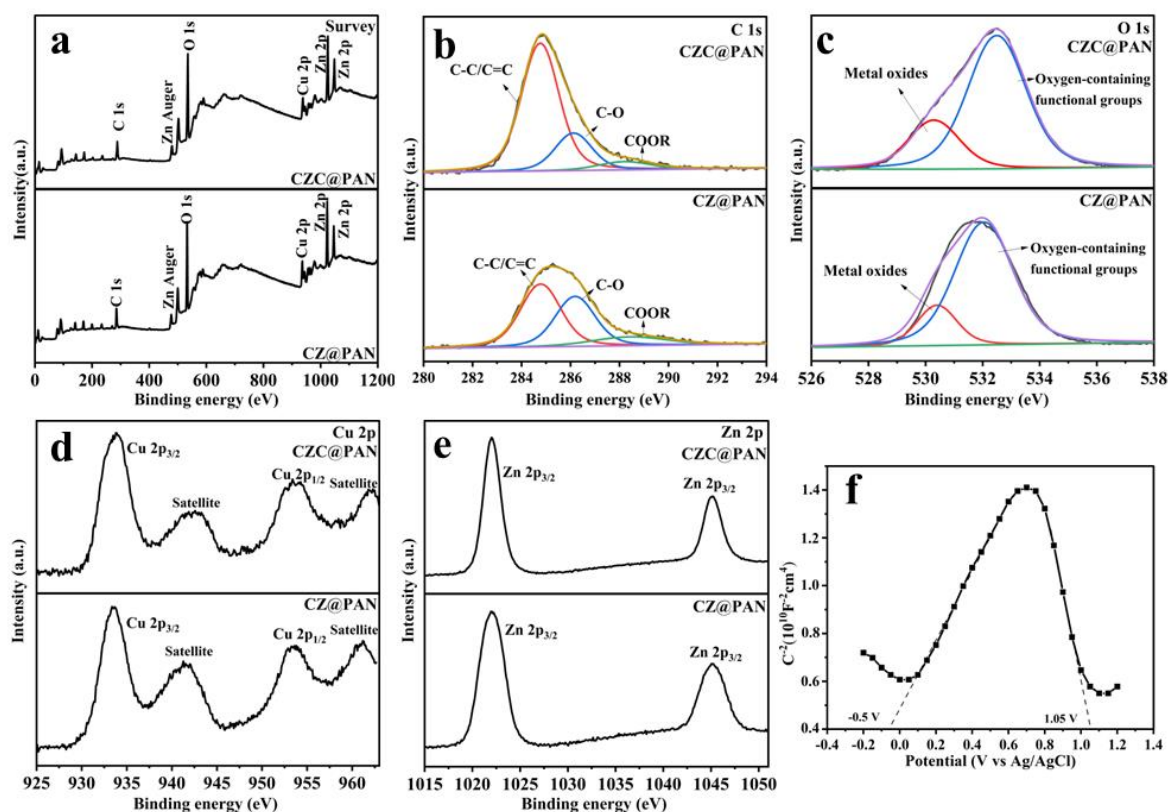


Figure 2. XPS spectra of samples: survey (a), C 1s (b), O 1s (c), Cu 2p (d), and Zn 2p (e); Mott-Schottky curve of CZC@PAN (f).

To further determine the electronic energy band structure of CZC@PAN, a Mott-Schottky test was performed, and the Mott-Schottky curve was shown in Figure 2f. In general, an n-type or p-type semiconductor can be determined by the slope of the linear part of its Mott-Schottky curve, where a positive slope represents an n-type semiconductor and a negative slope indicates a p-type semiconductor. The results showed that the appearance of positive and negative slopes in the Mott-Schottky curve of CZC@PAN was a typical p-n junction feature [42], which was in complete agreement with the XPS and TEM analyses. In addition, in our previous work [5], the Mott-Schottky curve of CZ@PAN indicated that CZ@PAN was also a typical p-n junction, which illustrated that CQDs had no effect on the energy band structure of CZC@PAN.

2.4. UV-vis and PL Analysis

Compared with CZ@PAN, CZC@PAN demonstrated stronger response and a considerable red-shifted absorption edge in the visible light region (Figure 3a). According to Tauc plot (Figure 3b), the band gap energy of CZ@PAN and CZC@PAN was close, verifying that there was no new energy band structure in CZC@PAN compared with CZ@PAN, including a new bandgap formed. When the excitation wavelength was 370 nm, the fluorescence intensity of CZC@PAN was lower than that of CZ@PAN, indicating that the loading of CQDs was more helpful to hinder the recombination of photogenerated electron-hole pairs (Figure 3c). The above results showed that CZC@PAN had better photocatalytic performance than CZ@PAN.

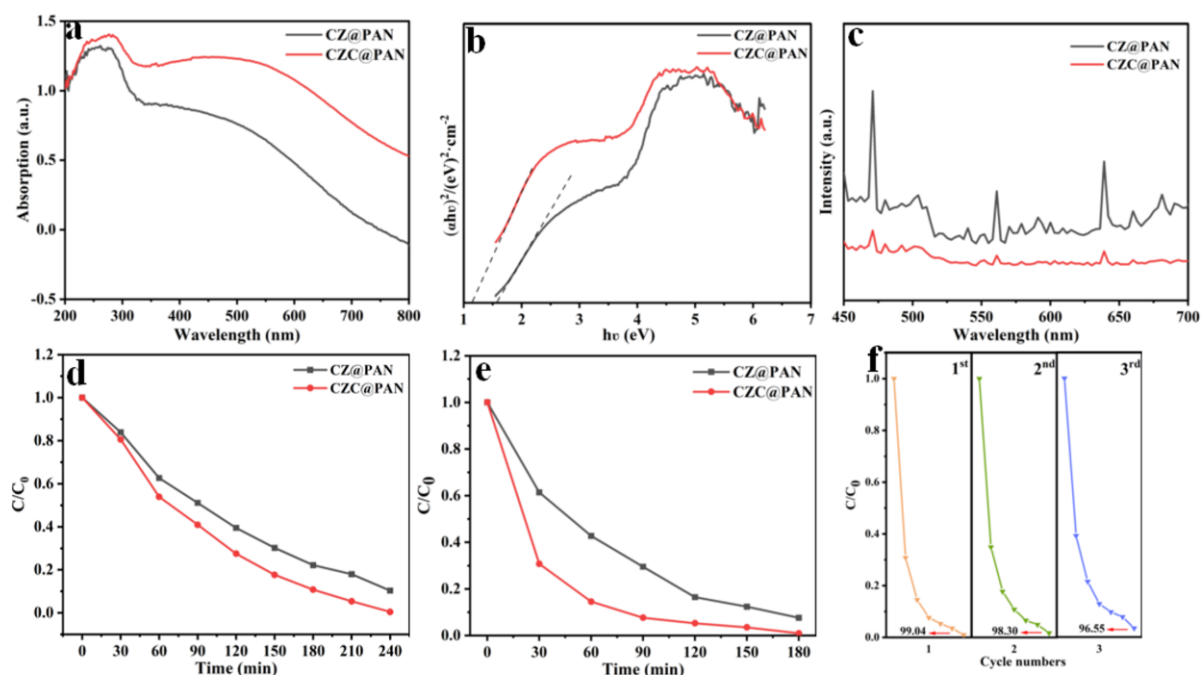


Figure 3. UV-vis spectra (a), Tauc plot (b), PL spectra (c), photocatalytic degradation of MB under natural sunlight (d), photocatalytic degradation of MB under mercury lamp (e) of samples; Reuse efficiency of CZC@PAN under mercury lamp (f).

2.5. Photocatalytic Degradation Performance

Under natural sunlight, the degradation rates of CZ@PAN and CZC@PAN were separately 89.67% and 99.56% after degrading MB for 4 h (Figure 3d), showing their good photocatalytic degradation effects. Moreover, CQDs further enhanced the absorption of sunlight and promoted the separation and transfer of electron-hole pairs, thus improving the photocatalytic degradation performance of samples. Under mercury lamp, the degradation rates of CZ@PAN and CZC@PAN reached 70.49% and 92.36%, respectively, after 1.5 h of MB degradation, while their degradation rates of MB solution reached 92.39% and 99.04% respectively after 3 h (Figure 3e). After three repeated experiments, the degradation rate of MB by CZC@PAN for 3 h was still 96.55% (Figure 3f), illustrating that it had good reusability.

2.6. Photocatalytic Degradation Mechanism

Free radical capture experiments illustrated the addition of BQ reduced the photodegradation rate of MB to 61%, while the addition of IPA and AO reduced the photodegradation rate to 87.10% and 84.24%, respectively (Figure 4a). Therefore, $\cdot\text{O}_2^-$ was the main active group, while $\cdot\text{OH}$ and photogenerated h^+ contributed relatively less to the MB degradation. Based on the above characterization and analysis, a photocatalytic degradation mechanism of CZC@PAN was presented, as shown in Figure 4b. The con-

duction band (CB) potentials for CuO and ZnO were -0.43 eV and -0.15 eV vs. normal hydrogen electrode (NHE), respectively, while the band gaps of CuO and ZnO were 1.4 eV and 3.23 eV, respectively [30]. Therefore, the valence band (VB) potentials for CuO and ZnO were 0.97 eV and 3.08 eV, respectively. When CuO/ZnO/CQDs heterostructures were exposed to sunlight, the photogenerated electrons (e^-) on the CB of CuO migrated to the CB of ZnO, while the h^+ on the VB of ZnO transferred to the VB of CuO, resulting in many photoexcited electron–hole pairs on CuO/ZnO heterostructures, effectively separating the photogenerated carriers through the p-n heterostructures, and extending the light response range of ZnO from the UV region to the visible region [5,30,43]. Meanwhile, the up-converted PL behavior of CQDs can further broaden the light utilization range of CuO/ZnO, excite CuO/ZnO to form more photogenerated electron–hole pairs [35,36]. Besides, CQDs could not only boost e^- transfer to the surface of CuO/ZnO heterostructures, but also transfer excess e^- from CuO/ZnO heterostructures to CQDs, thus improving the separation rate of electron–hole pairs [14–18,22,44,45]. Then, through redox reactions, O_2 adsorbed on the catalyst surface captured e^- to produce $\cdot O_2^-$ (-0.33 eV vs. NHE) and h^+ combined with H_2O to generate $\cdot OH$ (2.68 eV vs. NHE) [46], which oxidized organic pollutants into CO_2 and H_2O , resulting in higher photocatalytic activity.

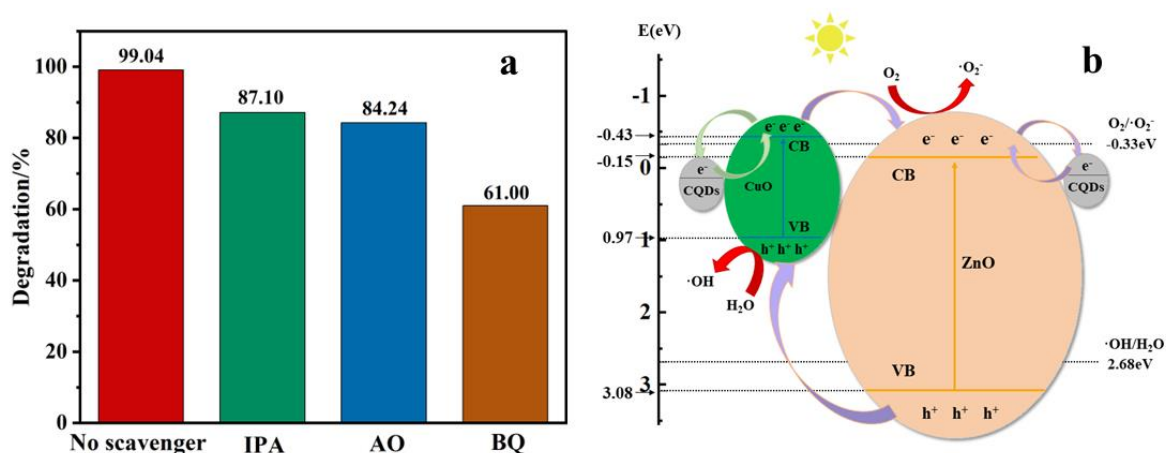


Figure 4. Free radical trapping experiment results (a) and photocatalytic degradation mechanism (b) of CZC@PAN.

3. Materials and Methods

3.1. Materials

Polyacrylonitrile (PAN, $Mw = 150,000$ g/mol) powders were offered from Hefei Sipin Technology Co., Ltd. (Hefei, China). *N,N*-dimethylformamide (DMF, $Mw = 73.09$ g/mol) was obtained from Shanghai Chemical Reagent Co., Ltd. (Shanghai, China). Graphite rods were provided by Alfa Aesar Co., Ltd. (Tianjin, China). Anhydrous zinc acetate ($Zn(Ac)_2$, $Mw = 183.48$ g/mol) and anhydrous copper acetate ($Cu(Ac)_2$, $Mw = 181.63$ g/mol) were purchased from Shanghai Aladdin Biochemical Co., Ltd. (Shanghai, China). Copper sulphate ($CuSO_4$, $Mw = 159.60$ g/mol), ammonia ($NH_3 \cdot H_2O$, $Mw = 17.03$ g/mol), hexamethylenetetramine (HMTA, $Mw = 140.19$ g/mol), and zinc chloride ($ZnCl_2$, $Mw = 136.30$ g/mol) were purchased from China Pharmaceutical Group Chemical Reagents Co., Ltd. (Shanghai, China). Methylene blue (MB, $Mw = 373.90$ g/mol) was supplied by Shanghai Debai Biotechnology Co., Ltd. (Shanghai, China). Sodium sulphate (Na_2SO_4 , $Mw = 142.04$ g/mol) and isopropyl alcohol (IPA, $Mw = 60.01$ g/mol) were provided by Jiangsu Qiangsheng Functional Chemical Co., Ltd. (Suzhou, China). Ammonium oxalate (AO) was supplied by Jiangsu Argon Krypton Xenon Material Technology Co., Ltd. (Suzhou, China). *P*-benzoquinone (BQ) was obtained from Suzhou Grete Pharmaceutical Technology Co., Ltd. (Suzhou, China).

3.2. Preparation of CZC@PAN

As shown in Figure 5, firstly, $\text{Cu}(\text{Ac})_2/\text{Zn}(\text{Ac})_2/\text{PAN}$ composite NFMs ($\text{Cu}(\text{Ac})_2/\text{Zn}(\text{Ac})_2/\text{PAN}$ -CNFMs) were prepared by electrospinning, and then the carbon NFMs containing CuO/ZnO nanoparticles (CZ-NPs-CNFMs) were obtained by heat treatment. Finally, CZC@PAN was hydrothermally synthesized by adding CQDs to the growth solution. As a control, CuO/ZnO @PAN nanocomposites (CZ@PAN) were hydrothermally synthesized using a growth solution without CQDs.

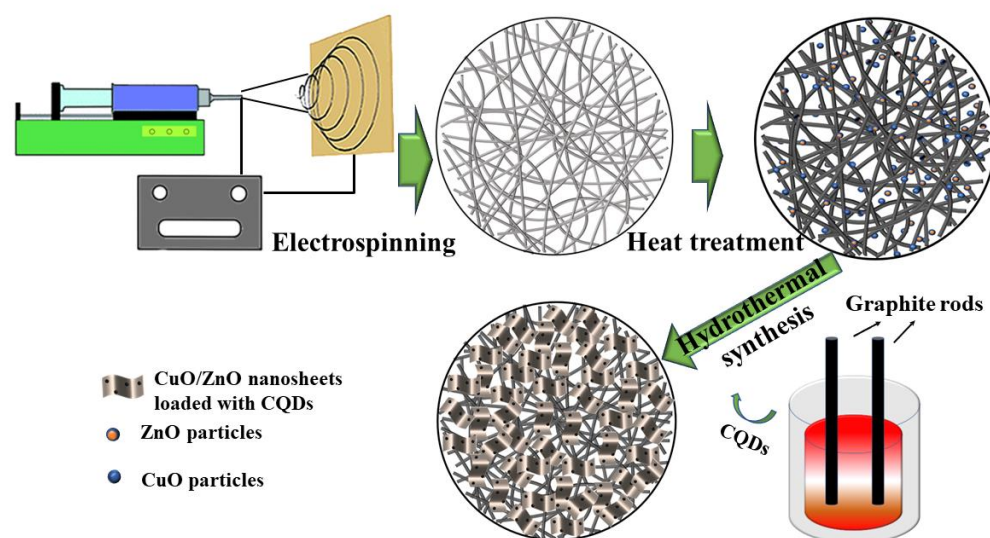


Figure 5. Preparation flowchart of CZC@PAN.

3.2.1. Preparation of CZ-NPs-CNFMs

4 g PAN was weighed and dissolved in 46 g DMF, and then 4 g $\text{Cu}(\text{Ac})_2$ and 4 g $\text{Zn}(\text{Ac})_2$ were weighed and added into the aforementioned solution and thoroughly mixed. Next, $\text{Cu}(\text{Ac})_2/\text{Zn}(\text{Ac})_2/\text{PAN}$ -CNFMs were prepared by electrospinning at a spinning distance of 15 cm, a flow parameter of 0.6 mL h^{-1} , and a voltage of 15 kV. Finally, these composite NFMs were cut into $3 \times 3 \text{ cm}$ squares and heated at $150 \text{ }^\circ\text{C}$ for 3 h to produce CZ-NPs-CNFMs.

3.2.2. Preparation of CQD Solution and Growth Solution

Firstly, CQD solution were fabricated by electrochemical etching of graphite rods [47]. 1 mL of the prepared CQD solution was mixed with 2 mL of deionized water by sonicate for 10 min to obtain the diluted CQD solution for subsequent use. Next, 2 g of ZnCl_2 and 2 g of CuSO_4 were put into two beakers respectively, and 10 mL of deionized water was added into each beaker. After ZnCl_2 and CuSO_4 in the two beakers were completely dissolved, 10 mL of ammonia was added dropwise into each beaker and uniformly mixed. Then the solutions in the two beakers were mixed in one beaker and stirred evenly to obtain the growth solution without CQDs. Finally, $300 \text{ }\mu\text{L}$ of CQD solution was mixed with 20 mL of the above prepared growth solution by sonicate for 10 min to obtain the growth solution with CQDs.

3.2.3. Preparation of CZC@PAN

CZ-NPs-CNFMs were immersed in a reactor containing the growth solution with CQDs. Afterwards, the reactor was put into an electrothermal thermostatic blast drying oven for hydrothermal synthesis at $150 \text{ }^\circ\text{C}$ for 3 h to obtain CZC@PAN. Finally, CZC@PAN was taken out from the reactor, washed with deionized water, and dried. Similarly, CZ@PAN was obtained using the growth solution without CQDs as a control.

3.3. Measurement and Characterization

The morphology and elemental distribution of samples were studied by a scanning electron microscopy (SEM, Regulus 8100, Tokyo, Japan) equipped with an energy dispersive spectroscopy (EDS) and a transmission electron microscopy (TEM, HT7700, Tokyo, Japan). The lattice spacing of samples was observed by a high-resolution transmission electron microscopy (HRTEM, Tecnai G2 F20 S-Twin, Portland Oregon, USA). Fourier transform infrared (FTIR) patterns of samples were tested by a FTIR spectrometer (Nicolet 5700, Thermo Nicolet Company, New York, NY, USA). The crystal structure of samples was characterized by X-ray diffraction (XRD) analysis (D8 Advance, Karlsruhe, Germany). The chemical composition of samples was analyzed by an X-ray photoelectron spectroscopy (XPS, Axis Ultra DLD, Manchester, UK). Mott–Schottky testing was performed by an electrochemical workstation (CHI660E, Chenhua, Shanghai, China). The light absorption ability of samples was tested through an UV-vis-NIR spectrometer (UV3600, Tokyo, Japan). The photoluminescence (PL) spectra of samples were tested by a fluorescence spectrometer (FLS920, Edinburgh, UK).

3.4. Photocatalytic Degradation Tests

The photocatalytic properties of samples were investigated by degrading MB solution under a UV lamp (250 W, 365 nm) and natural sunlight, respectively. In order to achieve the adsorption–desorption equilibrium, 0.1 g of the sample was placed in 40 mL of MB solution (10 mg L^{-1}) and kept in the dark for 1 h. The maximum absorbance of the MB solution was measured using a UV-vis spectrophotometer (SPECORD S600, Jena, Germany) at 664 nm for various time intervals. Free radical capture studies were performed to discover the main active components in the photocatalytic degradation of MB. 0.01 M of IPA, AO, and BQ were added to MB solutions as trapping agents respectively to capture hydroxyl radicals ($\cdot\text{OH}$), photogenerated holes (h^+), and superoxide radicals ($\cdot\text{O}_2^-$) correspondingly.

4. Conclusions

A nanophotocatalyst with ternary heterostructures (CZC@PAN) was fabricated, characterized, and applied in the photocatalytic degradation of MB. The synergistic effects of components in ternary heterostructures on the morphology, structure, and photocatalytic activity of CZC@PAN were further discussed. It was found that the photocatalytic degradation rate of MB by CZC@PAN was 99.04% under mercury lamp for 3 h and 99.56% under natural sunlight for 4 h, respectively. Compared with CZ@PAN, CZC@PAN could broaden the light utilization range and separate photogenerated electron-hole pairs faster, leading to its better photocatalytic performance. The high photocatalytic activity of CZC@PAN might be related to the creation of p-n heterojunctions and the loading of CQDs, which promoted the photo response ability of CZC@PAN and its separation rate of photogenerated electron-hole pairs, making it a high-performance environmentally friendly nanophotocatalyst.

Author Contributions: Conceptualization, H.X. and L.X.; Methodology, H.X. and L.X.; Validation, H.X. and P.F.; Formal analysis, H.X. and P.F.; Investigation, H.X. and P.F.; Resources, L.X.; Data curation, H.X. and P.F.; Writing—original draft preparation, H.X. and P.F.; Writing—review and editing, L.X.; Supervision, L.X.; Project administration, L.X.; Funding acquisition, L.X. All authors have read and agreed to the published version of the manuscript.

Funding: This research was funded by National Natural Science Foundation of China (grant number 11672198), Jiangsu Higher Education Institutions of China (grant number 20KJA130001), Jiangsu Engineering Research Center of Textile Dyeing and Printing for Energy Conservation (grant number ERC-Q811580722), and PAPD (A Project Funded by the Priority Academic Program Development of Jiangsu Higher Education Institutions).

Data Availability Statement: Not applicable.

Conflicts of Interest: The authors declare no conflict of interest.

References

1. Wen, X.J.; Shen, C.-H.; Fei, Z.H.; Fang, D.; Liu, Z.T.; Dai, J.T.; Niu, C.G. Recent developments on AgI based heterojunction photocatalytic systems in photocatalytic application. *Chem. Eng. J.* **2020**, *383*, 123083. [\[CrossRef\]](#)
2. Koe, W.S.; Lee, J.W.; Chong, W.C.; Pang, Y.L.; Sim, L.C. An overview of photocatalytic degradation: Photocatalysts, mechanisms, and development of photocatalytic membrane. *Environ. Sci. Pollut. Res.* **2020**, *27*, 2522–2565. [\[CrossRef\]](#) [\[PubMed\]](#)
3. Wang, X.; Li, S.; Chen, P.; Li, F.; Hu, X.; Hua, T. Photocatalytic and antifouling properties of TiO₂-based photocatalytic membranes. *Mater. Today Chem.* **2022**, *23*, 100650. [\[CrossRef\]](#)
4. Zhang, T.; Dai, Z.; Liang, B.; Mu, Y. Facile Synthesis of SnO₂/SiC nanosheets for photocatalytic degradation of MO. *J. Inorg. Organomet. Polym. Mater.* **2021**, *31*, 303–310. [\[CrossRef\]](#)
5. Xu, H.; Fang, W.; Xu, L.; Liu, F. Batch preparation of CuO/ZnO-loaded nanofiber membranes for photocatalytic degradation of organic dyes. *Langmuir* **2020**, *36*, 14189–14202. [\[CrossRef\]](#)
6. Dlugosz, O.; Wąsowicz, N.; Szostak, K.; Banach, M. Photocatalytic properties of coating materials enriched with bentonite/ZnO/CuO nanocomposite. *Mater. Chem. Phys.* **2021**, *260*, 124150. [\[CrossRef\]](#)
7. Cheng, X.; Li, L.; Jia, L.; Cai, H.; Wang, X.; Ding, Y.; Fan, X. Preparation of K⁺ doped ZnO nanorods with enhanced photocatalytic performance under visible light. *J. Phys. D Appl. Phys.* **2019**, *53*, 035301. [\[CrossRef\]](#)
8. Liu, H.; Gu, H.; Li, G.; Li, N. Fabrication of PAN/Ag/ZnO microporous membrane and examination of visible light photocatalytic performance. *Fiber Polym.* **2021**, *22*, 306–313. [\[CrossRef\]](#)
9. Xu, M.; Wang, H.; Wang, G.; Zhang, L.; Liu, G.; Zeng, Z.; Ren, T.; Zhao, W.; Wu, X.; Xue, Q. Study of synergistic effect of cellulose on the enhancement of photocatalytic activity of ZnO. *J. Mater. Sci.* **2017**, *52*, 8472–8484. [\[CrossRef\]](#)
10. Sabouni, R.; Gomaa, H. Photocatalytic degradation of pharmaceutical micro-pollutants using ZnO. *Environ. Sci. Pollut. Res.* **2019**, *26*, 5372–5380. [\[CrossRef\]](#)
11. Kayaci, F.; Vempati, S.; Ozgit-Akgun, C.; Biyikli, N.; Uyar, T. Enhanced photocatalytic activity of homoassembled ZnO nanostructures on electrospun polymeric nanofibers: A combination of atomic layer deposition and hydrothermal growth. *Appl. Catal. B Environ.* **2014**, *156–157*, 173–183. [\[CrossRef\]](#)
12. Li, S.; Chu, D.; Wang, L.; Rong, R.; Zhang, N. One-step hydrothermal synthesis of CuO hollow spheres with high photocatalytic activity. *Phys. E* **2021**, *126*, 114489. [\[CrossRef\]](#)
13. Xu, L.; Su, J.; Zheng, G.; Zhang, L. Enhanced photocatalytic performance of porous ZnO thin films by CuO nanoparticles surface modification. *Mater. Sci. Eng. B* **2019**, *248*, 114405. [\[CrossRef\]](#)
14. Liang, H.; Tai, X.; Du, Z.; Yin, Y. Enhanced photocatalytic activity of ZnO sensitized by carbon quantum dots and application in phenol wastewater. *Opt. Mater.* **2020**, *100*, 109674. [\[CrossRef\]](#)
15. Li, J.; Liu, K.; Xue, J.; Xue, G.; Sheng, X.; Wang, H.; Huo, P.; Yan, Y. CQDS precluded carbon-incorporated 3D burger-like hybrid ZnO enhanced visible-light-driven photocatalytic activity and mechanism implication. *J. Catal.* **2019**, *369*, 450–461. [\[CrossRef\]](#)
16. Behnood, R.; Sodeifian, G. Synthesis of N doped-CQDs/Ni doped-ZnO nanocomposites for visible light photodegradation of organic pollutants. *J. Environ. Chem. Eng.* **2020**, *8*, 103821. [\[CrossRef\]](#)
17. Ding, D.; Lan, W.; Yang, Z.; Zhao, X.; Chen, Y.; Wang, J.; Zhang, X.; Zhang, Y.; Su, Q.; Xie, E. A simple method for preparing ZnO foam/carbon quantum dots nanocomposite and their photocatalytic applications. *Mater. Sci. Semicond. Process.* **2016**, *47*, 25–31. [\[CrossRef\]](#)
18. Gao, D.; Zhao, P.; Lyu, B.; Li, Y.; Hou, Y.; Ma, J. Carbon quantum dots decorated on ZnO nanoparticles: An efficient visible-light responsive antibacterial agents. *Appl. Organomet. Chem.* **2020**, *34*, e5665. [\[CrossRef\]](#)
19. Zhang, J.; An, X.; Li, X.; Liao, X.; Nie, Y.; Fan, Z. Enhanced antibacterial properties of the bracket under natural light via decoration with ZnO/carbon quantum dots composite coating. *Chem. Phys. Lett.* **2018**, *706*, 702–707. [\[CrossRef\]](#)
20. Vyas, Y.; Chundawat, P.; Dharmendra; Punjabi, P.B.; Ameta, C. Green and facile synthesis of luminescent CQDs from pomegranate peels and its utilization in the degradation of azure B and amido black 10B by decorating it on CuO nanorods. *ChemistrySelect* **2021**, *6*, 8566–8580. [\[CrossRef\]](#)
21. Li, Z.; Zhou, L.; Lu, L.; Xu, X.; Jiang, Y. Enhanced photocatalytic properties of ZnO/Al₂O₃ nanorod heterostructure. *Mater. Res. Express* **2021**, *8*, 045505. [\[CrossRef\]](#)
22. Fu, L.X.; Guo, Y.; Yang, X.C.; Huang, J.; Wang, L.J. Carbon dots modifier for highly active photocatalysts based on ZnO porous microspheres. *J. Mater. Sci. Mater. Electron.* **2018**, *29*, 19994–20002. [\[CrossRef\]](#)
23. Tasso, G.T.; Wenk, J.; Mattia, D. Photocatalytic ZnO Foams for micropollutant degradation. *Adv. Sustain. Syst.* **2021**, *5*, 2000208. [\[CrossRef\]](#)
24. Karimi, S.M.; Behpour, M. Fabricated CuO-ZnO/nanozeolite X heterostructure with enhanced photocatalytic performance: Mechanism investigation and degradation pathway. *Mater. Sci. Eng. B* **2021**, *269*, 115170. [\[CrossRef\]](#)
25. Kim, H.Y.; Ju, Y.W. Influence of post-heat treatment on photocatalytic activity in metal-embedded TiO₂ nanofibers. *Korean J. Chem. Eng.* **2021**, *38*, 1522–1528. [\[CrossRef\]](#)
26. Liu, Y.; Jia, J.; Li, Y.V.; Hao, J.; Pan, K. Novel ZnO/NiO Janus-like nanofibers for effective photocatalytic degradation. *Nanotechnology* **2018**, *29*, 435704. [\[CrossRef\]](#)
27. Alias, N.H.; Jaafar, J.; Samitsu, S.; Yusof, N.; Othman, M.H.D.; Rahman, M.A.; Ismail, A.F.; Aziz, F.; Salleh, W.N.W.; Othman, N.H. Photocatalytic degradation of oilfield produced water using graphitic carbon nitride embedded in electrospun polyacrylonitrile nanofibers. *Chemosphere* **2018**, *204*, 79–86. [\[CrossRef\]](#)

28. Lakshmi, K.; Kadirvelu, K.; Mohan, P.S. Photo-decontamination of p-nitrophenol using reusable lanthanum doped ZnO electrospun nanofiber catalyst. *J. Mater. Sci. Mater. Electron.* **2018**, *29*, 12109–12117. [[CrossRef](#)]
29. Tuncel, D.; Ökte, A.N. ZnO@CuO derived from Cu-BTC for efficient UV-induced photocatalytic applications. *Catal. Today* **2019**, *328*, 149–156. [[CrossRef](#)]
30. Sakib, A.A.; Masum, S.M.; Hoinkis, J.; Islam, R.; Molla, M.A. Synthesis of CuO/ZnO nanocomposites and their application in photodegradation of toxic textile dye. *J. Compos. Sci.* **2019**, *3*, 91. [[CrossRef](#)]
31. Tissera, N.D.; Wijesena, R.N.; Sandaruwan, C.S.; de Silva, R.M.; de Alwis, A.; de Silva, K.M.N. Photocatalytic activity of ZnO nanoparticle encapsulated poly(acrylonitrile) nanofibers. *Mater. Chem. Phys.* **2018**, *204*, 195–206. [[CrossRef](#)]
32. Chen, Y.Y.; Kuo, C.C.; Chen, B.Y.; Chiu, P.C.; Tsai, P.C. Multifunctional polyacrylonitrile-ZnO/Ag electrospun nanofiber membranes with various ZnO morphologies for photocatalytic, UV-shielding, and antibacterial applications. *J. Polym. Sci. Polym. Phys.* **2015**, *53*, 262–269. [[CrossRef](#)]
33. Wang, H.Y.; Yang, Y.; Li, X.; Li, L.J.; Wang, C. Preparation and characterization of porous TiO₂/ZnO composite nanofibers via electrospinning. *Chin. Chem. Lett.* **2010**, *21*, 1119–1123. [[CrossRef](#)]
34. Fang, W.; Yu, L.; Xu, L. Preparation, characterization and photocatalytic performance of heterostructured CuO-ZnO-loaded composite nanofiber membranes. *Beilstein J. Nanotechnol.* **2020**, *11*, 631–650. [[CrossRef](#)] [[PubMed](#)]
35. Yu, H.; Zhang, H.; Huang, H.; Liu, Y.; Li, H.; Ming, H.; Kang, Z. ZnO/carbon quantum dots nanocomposites: One-step fabrication and superior photocatalytic ability for toxic gas degradation under visible light at room temperature. *New J. Chem.* **2012**, *36*, 1031–1035. [[CrossRef](#)]
36. Li, Y.; Zhang, B.P.; Zhao, J.X.; Ge, Z.H.; Zhao, X.K.; Zou, L. ZnO/carbon quantum dots heterostructure with enhanced photocatalytic properties. *Appl. Surf. Sci.* **2013**, *279*, 367–373. [[CrossRef](#)]
37. Raula, M.; Rashid, M.H.; Paira, T.K.; Dinda, E.; Mandal, T.K. Ascorbate-Assisted Growth of Hierarchical ZnO Nanostructures: Sphere, Spindle, and Flower and Their Catalytic Properties. *Langmuir* **2010**, *26*, 8769–8782. [[CrossRef](#)]
38. Alias, N.H.; Jaafar, J.; Samitsu, S.; Ismail, A.F.; Mohamed, M.A.; Othman, M.H.D.; Rahman, M.A.; Othman, N.H.; Nor, N.A.M.; Yusof, N.; et al. Mechanistic insight of the formation of visible-light responsive nanosheet graphitic carbon nitride embedded polyacrylonitrile nanofibres for wastewater treatment. *J. Water Process. Eng.* **2020**, *33*, 101015. [[CrossRef](#)]
39. Liang, Q.; Li, Z.; Bai, Y.; Huang, Z.H.; Kang, F.; Yang, Q.H. Reduced-sized monolayer carbon nitride nanosheets for highly improved photoresponse for cell imaging and photocatalysis. *Sci. China Mater.* **2017**, *60*, 109–118. [[CrossRef](#)]
40. Bellini, J.V.; Machado, R.; Morelli, M.R.; Kiminami, R.H.G.A. Thermal, Structural and Morphological Characterisation of Freeze-dried Copper(II) Acetate Monohydrate and its Solid Decomposition Products. *Mater. Res.* **2002**, *5*, 453–457. [[CrossRef](#)]
41. Baláž, P.; Aláčová, A.; Achimovičová, M.; Ficeriová, J.; Godočíková, E. Mechanochemistry in hydrometallurgy of sulphide minerals. *Hydrometallurgy* **2005**, *77*, 9–17. [[CrossRef](#)]
42. Zhu, L.; Li, H.; Liu, Z.; Xia, P.; Xie, Y.; Xiong, D. Synthesis of the 0D/3D CuO/ZnO Heterojunction with Enhanced Photocatalytic Activity. *J. Phys. Chem. C* **2018**, *122*, 9531–9539. [[CrossRef](#)]
43. Ni, M.; Zhang, H.; Khan, S.; Chen, X.; Chen, F.; Guo, C.; Zhong, Y.; Hu, Y. In-situ photodeposition of cadmium sulfide nanocrystals on manganese dioxidenanorods with rich oxygen vacancies for boosting water-to-oxygen photooxidation. *J. Colloid Interface Sci.* **2022**, *613*, 764–774. [[CrossRef](#)]
44. Roza, L.; Fauzia, V.; Rahman, M.Y.A.; Isnaeni, I.; Putro, P.A. ZnO nanorods decorated with carbon nanodots and its metal doping as efficient photocatalyst for degradation of methyl blue solution. *Opt. Mater.* **2020**, *109*, 110360. [[CrossRef](#)]
45. Zhou, M.; Hu, Y.; Liu, Y.; Yang, W.; Qian, H. Microwave-assisted route to fabricate coaxial ZnO/C/CdS nanocables with enhanced visible light-driven photocatalytic activity. *CrystEngComm* **2012**, *14*, 7686–7693. [[CrossRef](#)]
46. Malik, J.; Kumar, S.; Srivastava, P.; Bag, M.; Mandal, T.K. Cation disorder and octahedral distortion control of internal electric field, band bending and carrier lifetime in Aurivillius perovskite solid solutions for enhanced photocatalytic activity. *Mater. Adv.* **2021**, *2*, 4832. [[CrossRef](#)]
47. Ming, H.; Ma, Z.; Liu, Y.; Pan, K.; Yu, H.; Wang, F.; Kang, Z. Large scale electrochemical synthesis of high quality carbon nanodots and their photocatalytic property. *Dalton Trans.* **2012**, *41*, 9526–9531. [[CrossRef](#)]

Disclaimer/Publisher's Note: The statements, opinions and data contained in all publications are solely those of the individual author(s) and contributor(s) and not of MDPI and/or the editor(s). MDPI and/or the editor(s) disclaim responsibility for any injury to people or property resulting from any ideas, methods, instructions or products referred to in the content.